# Mesoporous Spongy Ni-Co-Oxides@Wheat Straw-Derived SiO2 For Adsorption And Photocatalytic Degradation of Methylene Blue Pollutants

**Mohamed A. T. Hussein**
Al-Azhar University - Assiut Branch
**Mohamed M Motawea**
Al-Azhar University - Assiut Branch
**Mohamed M. Elsenety**
Al-Azhar University Faculty of Science
**Salah M. El-Bahy**
Taif University
**Hassanien Gomaa** ( h.gomaa@azhar.edu.eg )
Al-Azhar University - Assiut Branch https://orcid.org/0000-0002-7470-7741

**Research Article**

**Keywords:** Ni-Co-oxides, wheat straw-derived SiO2, MWSS, methylene blue, adsorption, photocatalytic degradation, mesoporous

**Posted Date:** August 17th, 2021

**DOI:** https://doi.org/10.21203/rs.3.rs-780301/v1



**Version of Record:** A version of this preprint was published at Applied Nanoscience on January 29th, 2022. See the published version at https://doi.org/10.1007/s13204-021-02318-0.

# Mesoporous spongy Ni-Co-oxides@wheat straw-derived $SiO_2$ for adsorption and photocatalytic degradation of methylene blue pollutants

Mohamed A. T. Hussein[1], Mohamed M. Motawea[1], Mohamed M. Elsenety[2], Salah M. El-Bahy[3], Hassanien Gomaa[1]*

[1]Department of Chemistry, Faculty of Science, Al-Azhar University, 71524 Assiut, Egypt.

[2]Department of Chemistry, Faculty of Science, Al-Azhar University, 11823, Cairo, Egypt.

[3]Department of Chemistry, Turabah University College, Taif University, P.O.Box 11099, Taif 21944, Saudi Arabia.

*Email (H. gomaa): h.gomaa@azhar.edu.eg

**Abstract:**

The exploitation and employment of agricultural waste in polluted water treatment is one of the most important cost-effective approaches. Therefore, a novel mesoporous spongy adsorbent/photocatalyst was successfully synthesized through the grafting of nickel and cobalt oxides nanocomposites with wheat straw-derived $SiO_2$. Nickel and cobalt oxides were added to enhance the functionality of wheat straw-derived $SiO_2$. This synthesis methodology presents a simplistic, cost-effective, and eco-approachable alternative to getting an adsorbent and photocatalyst for the adsorption and photocatalytic degradation of methylene blue (MB) pollutants from wastewater. The modified wheat straw-derived $SiO_2$ (MWSS) was characterized via XRD, SEM, EDX, TGA, FTIR, and nitrogen adsorption. Molecular dynamics computational calculations were performed to comprehend the ability of methylene blue to adjust the WSDS surface. The experiments of adsorption and photodegradation trials were performed to optimize the pH, contact time, initial MB-concentration, and temperature parameters. Furthermore, kinetics and isotherm models were checked to explain the MB-removal mechanism using mesoporous spongy MWSS. The current work indicated that the

mesoporous MWSS adsorbent/photocatalyst provided efficient adsorption capability (79%), significant photocatalytic performance (93%), and higher solidity during reusability as well. This study suggests an efficient composite that contributes to getting rid of the MB pollutants from wastewater.

**Keywords:** Ni-Co-oxides; wheat straw-derived $SiO_2$; MWSS; methylene blue; adsorption; photocatalytic degradation; mesoporous.

## 1. Introduction:

Clean water is one of the essential daily requirements for both modern and developing countries. The need for clean water is increasing steadily due to the rapid population growth (Nordin et al. 2021; Sayed et al. 2021; Zhang et al. 2021). Dyes are aqueous-based toxins, and the color index has recently been expanded to include over 9000 different types of dyes. Dyes are used in several industries; however, textile manufacturing industries are the most popular users due to the market demand for attractive fabric colors (Islam et al. 2020; Hassan et al. 2021). While dyes have significant economic benefits, their excessive use pollutes the water supply. Since dyes are made up of organic compounds with large molecular weight, their discharge into water supplies poses significant environmental troubles (Li et al. 2021). Since certain dyes are carcinogenic and mutagenic, they damage both aquatic and human life (Zhou et al. 2017; Eren et al. 2020). As a result, the main environmental issue is the removal of dyes from polluted water.

Methylene blue (MB) can cause permanent damage to the skin and eyes and has some harmful properties on human beings such as inflammation of the mouth, throat, and stomach with symptoms of vomiting, nausea, delirium, diarrhea, and extreme perspiration (Bharti et al. 2019; Soni et al. 2020; Singh et al. 2021). Several water management solutions, such as physical, chemical, and biological, have been reported to regulate and mitigate water contamination.

Most of these methods have some disadvantages, such as high operational and maintenance costs, complicated processes, and the creation of hazardous sludge or by-products (Shaban et al. 2019; Balapure and Ganesan 2021). Because of their low cost, ease of operation, simplicity of design, environmentally friendly properties, and performance, adsorption and photocatalytic degradation over porous materials are considered the most suitable approaches for water cleansing (De Gisi et al. 2016; Gupta et al. 2016; Mohamed et al. 2017).

In the photocatalytic degradation methodology, the irradiation of a semiconductor, such as metal oxides, by UV-light produces some effective species such as electron-hole couples ($e^-/h^+$), hydroxyl ($^\bullet OH$), and superoxide ($^\bullet O_2^-$) radicals (Nemiwal et al. 2021). The mentioned species is a potent agent capable of attacking MB-molecules and breaking them down into more minor compounds through oxidation-reduction reactions (Ibrahim et al. 2020; Abdelwahab et al. 2020; Norouzi et al. 2021). As a result, the use of photocatalysts for environmental remediation has gained a lot of attention in recent years, as air and water contamination are potentially the most serious environmental threats to human health (Diaz et al. 2020; Naing et al. 2020). Mixed metal oxides are especially interesting because they allow the production of materials intermixed at the atomic level (Sun et al. 2020; Karuppusamy et al. 2021). Such structures can have chemical properties that are substantially different from those of single-component oxides. Therefore, Ni and Co oxide composite is vital for the current application (Chowdhury et al. 2010; Zhai et al. 2019; Emran et al. 2021).

Wheat straw is still deemed a waste by-product of wheat grinding, and hence, it is often burned in the open air. This practice of open burning involves energy waste and causes a serious environmental problem. Many scientists have concentrated their attempts to utilize wheat straw by exploiting its components, contemplating their large quantity and economical cost as agricultural trashes (Cui et al. 2015; Ahmad Alyosef et al. 2015; Chougan et al. 2020). Wheat straw-derived silica matrix is considered an ideal and excellent support material for catalyst

nanoparticles, leading to an increase in the surface area, decreasing used Ni-Co oxide amount, and improving photocatalytic activity in the long term (Ali et al. 2021; Seaf El-Nasr et al. 2021).

Herein, a novel mesoporous spongy MWSS was prepared to exploit the agricultural waste, such as wheat straw, for MB-adsorption and photocatalytic degradation from contaminated water. Parameters affecting the MB-adsorption and photocatalytic degradation efficiency towards removing MB dye using MWSS adsorbent/photocatalyst were explored, as well as kinetic and isotherm models. Our obtained data reveal that the mesoporous MWSS adsorbent/photocatalyst offers a sustainable solution for fast photodegradation and adsorption of MB-removal pollutants from wastewater even after multiple reuse cycles.

## 2. Experimental:

### 2.1.Materials

Nickel (II) chloride hexahydrate, cobalt (II) chloride hexahydrate, polyvinylpyrrolidone (PVP, average Molar mass 40,000 g/mol), methylene blue ($C_{16}H_{18}ClN_3S$, Molar mass 319.85 g/mol), and ethylene glycol (anhydrous, 99.8%) were bought from Sigma–Aldrich Company, Ltd., USA. Urea, ammonium hydroxide, sodium hydroxide, sulfuric acid, hydrochloric acid, and ethanol absolute were gained from Merck Chemicals Company, Germany. The consumed chemicals were high quality, so it was employed as obtained without additional cleansing.

### 2.2.Characterization tools

The calorimetric measurements were evaluated by a UV-Vis spectrophotometer (Evolution 300, Thermo Scientific, England). $N_2$ adsorption-desorption isotherms at 77° K were applied to explore the porosity and surface area of the mesoporous MWSS nanocomposite by using a St 1 on NOVAtouch 2LX analyzer. The surface morphology of the synthesized NiO&$Co_2O_3$ and MWSS nanocomposite was examined by scanning electron microscopy (SEM) using a

Carl Zeiss sigma 500 VP and JSM 5400 LV. The surface charge of MWSS nanocomposite was discovered using Zetasizer Nano ZS, Device Model: ZEN 3600, UK, Malvern. The structure durability of mesoporous MWSS nanocomposite at high temperatures was studied through thermal gravimetric and differential thermal analysis using DTG-60H, simultaneous DTA-TG apparatus, Shimadzu. High-resolution transmission electron microscopy (HRTEM) was used to investigate the nanostructures of $NiO\&Co_2O_3$ using JEM 100 CXII. The Wide-Angle X-ray diffraction (WA-XRD) using Bruker D8 Advance was used to verify the phase and crystal structure of $NiO\&Co_2O_3$ and MWSS nanocomposite. Fourier transform infrared (FTIR) spectra of the synthesized $NiO\&Co_2O_3$ and MWSS nanocomposite was achieved using a Nicolet IS10-PC scanning spectroscopy.

### 2.3.Synthesis of mesoporous spongyNi-Co-Oxides@wheat straw-derived $SiO_2$ (MWSS) nanocomposite:

(a) To prepare **Ni-Co-Oxides** composite, 2.5 g of nickel (II) chloride hexahydrate and 2.5 g of cobalt (II) chloride hexahydrate were dissolved in 100 mL of deionized water under continuous rousing for 2 hours, followed by adding 20 mL ethylene glycol. After an additional 1 hour under stirring, 1.5 g of PVP was inserted into the previous solution with continuous stirring for 2 hours. The resulting solution's pH was adjusted to pH = 10.0 using concentrated ammonium hydroxide solution to form nickel and cobalt hydroxides as a creamy solution. The achieved creamy solution was transferred to autoclave hydrothermal for 12 hours at 160$^{o}$C. The obtained precipitate was filtered, washed several times using ethanol, and deionized water to remove the unreacted components until getting a neutral residual solution (pH 7.0-7.5). After drying for 12 hours at 80 $^{o}$C, the as-made $Ni(OH)_2$ &$Co(OH)_2$ was calcined at 550 $^{o}$C under air conditions for 6 hours to gain Ni-Co oxide nanocomposite (see Scheme 1).

(b) At the same time, we have prepared the wheat straw-derived $SiO_2$ as follows: (i) the collected wheat straw was cleaned by faucet water to remove dust and else stacked impurities,

followed by the drying at 100ºC; (ii) the dried wheat straw was treated by 1M HCl at 80ºC under refluxing and stirring for 3 hours; (iii) After cooling, the treated wheat straw was filtered and washed by Milli-Q water till becoming free acid (i.e., near of neutral pH), and then dried at 80ºC for overnight; (iv) the obtained treated wheat straw was calcined at 700ºC for 6 hours to gain silica; (v) 5g of gained silica was entirely dissolved in 50mL of 1M NaOH at 70ºC under refluxing to obtain sodium silicate solution; (vi) the produced viscous solution was filtered, and then aged for further using.

(c) To prepare mesoporous MWSS nanocomposite, 3.0g of as-prepared NiO&$Co_2O_3$ was added to the sodium silicate solution and then stirred for 12 hours under high-speed stirring. The 50% sulfuric acid solution was added dropwise to the NiO&$Co_2O_3$@sodium silicate solution under constant stirring until the white silica formed at pH ~8, where the white precipitate MWSS nanocomposite can be formed. The obtained mesoporous MWSS nanocomposite was washed, dried, and then calcined at 550 ºC for 5 hours under air atmosphere. The nano-scaled mesoporous MWSS nanocomposite was stored in a black bottle for the subsequent experiments.

### 2.4.Bench-top adsorption and photocatalytic degradation processes for MB-removal:

In an adsorption test, 50 mg of MWSS nanocomposite was mixed with 50 mL of MB-dye solution in Erlenmeyer flasks at 500 rpm at various times and room temperature (~25±2°C). At pre-identified time intervals, residual MB-solution was filtered via centrifuge to separate the suspension MWSS material. The concentration of remained MB was verified using a UV–Vis spectrophotometer at $\lambda_{max}$ = 658 nm. In contrast, the photocatalytic degradation process was performed by mixing 50 mg of MWSS nanocomposite with 50 mL of MB-dye solution under stirring in a small dark room to reach the equilibrium adsorption stage. Then the MB-

degradation process was investigated under 70 W UV-lamp irradiation with a wavelength of 365 nm. The used UV-lamp was positioned at 10 cm from the reaction-contained flask. The MB-decolorization efficiency can be calculated using Eq.(1), while the adsorption capability of the MWSS ($q_e$, mg/g) can be determined using Eq.(2) (Abdien et al. 2016):

$$MB - decolorization\ \% = \frac{(C_i - C_f)}{C_i} \times 100 \qquad (1)$$

$$q_e = (C_i - C_f)\left(\frac{V}{w}\right) \qquad (2)$$

$C_i$ and $C_f$ (ppm or mg/L) are the initial and final MB-concentration before and after the removal process for both adsorption and photocatalytic degradation approaches. V is the volume of MB solution (L), and w is the mass of MWSS nanocomposite (g). Factors that can affect the MB-decolorization %, such as pH, time, temperature, etc., were systematically investigated. Furthermore, isotherm and kinetic studies were evaluated for both adsorption and photocatalytic degradation processes.

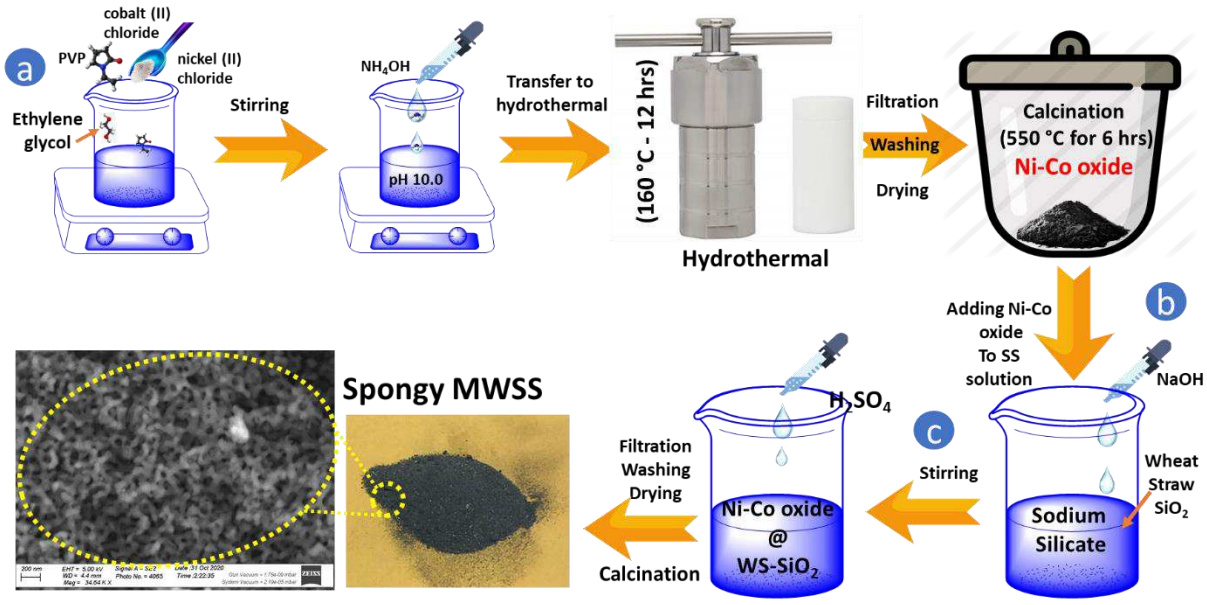


**Scheme 1.** Schematic design to show (a) preparation of Ni-Co oxide composite, (b) preparation of sodium silicate solution from wheat straw, (c) and grafting of Ni-Co oxide with sodium silicate to obtain mesoporous spongy MWSS.

### 2.5.Molecular dynamics calculations

The surfaces (001) were generated using the known SiO2 crystallographic structure of $SiO_2$ (Ji et al. 2020). The forcite module has been used with the COMPASS II force field for importing and optimizing structure to get energy minimization (Sun 1998; Phan et al. 2014; Sun et al. 2016). However, the optimized structure of WSDS was cleaved to produce (001) surface. The typical thickness of the surfaces was determined to consist of four $SiO_2$ layers parallel to the cleaved surfaces, and through geometrical optimization, the entire surface layers have been relaxed. 3D-simulation box with a size of (50.56 × 20.22 × 46.92 ˚A) was built from the surfaces to be able to include methylene blue molecules. In the case of Ni/Co Oxides@ WSDS, the Si positions on the top surface were modified by (Si 70.96%, Ni 15.12%, Co 13.91%) based on the experimental ratio out of EDX analysis. However, the 74 repeating units of methylene blue were geometry optimized using an amorphous cell module to fill the simulation box. Methylene blue unites were located at the top/down of each surface of WSDS and at least 5 ˚A afloat from the surface.

## 3. Results and discussion:

### 3.1.MWSS characterization

The crystallinity and phase purity of the prepared Ni-Co oxide composite and MWSS were explored using the XRD technique. XRD patterns of the Ni-Co oxide composite and MWSS have exhibited in Figure 1a&b. Figure 1a showed diffraction peaks at 2θ of 19°, 31°, 36.9°, 43°, 59.4°, 62.5°, 65.3°, 74.6°, 78.8° which corresponding to ●(111), ●(220), ●(311) and *(111), *(200), ●(511), *(220), ●(440), *(311), and *(222), where ● symbol is for $Co_3O_4$ peaks and *

symbol is for NiO peaks (Ramasamy et al. 2015), suggesting that the Ni-Co oxide composite was formed in two separate phases as $Co_3O_4$ and NiO. The reflection planes of $Co_3O_4$ and NiO indicated that both were prepared with a cubic crystal system (JCPDS no. 01-078-1969 and JCPDS no. 01-071-1179) as shown in figure 1(c,d). The broad-band in Figure 1b around 2θ of 15°-30° is assigned to the wheat straw-derived $SiO_2$ matrix's amorphous nature. The combined bands of Ni-Co oxide composite and wheat straw-derived $SiO_2$ in the XRD pattern validate the formation of MWSS. No extra peaks were identified in the XRD pattern, confirming the high structural purity of the prepared material.

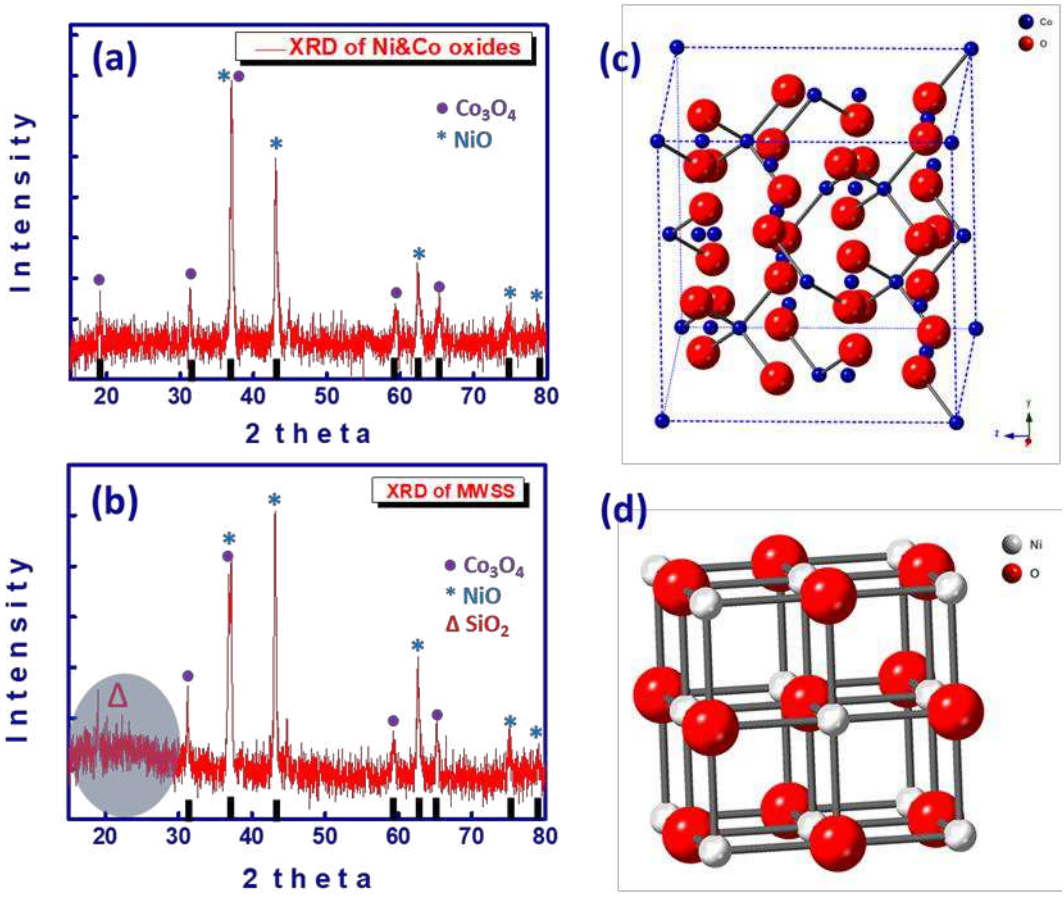


**Figure 1.** XRD of Ni-Co oxide composite (a), and mesoporous MWSS (b), cubic crystal structures of $Co_2O_3$ (c) and NiO (d)

The $N_2$ adsorption-desorption isotherm of the mesoporous spongy MWSS is demonstrated in Figure 2a to confirm the textural properties of MWSS, such as surface area and porosity. According to the IUPAC classification, the obtained isotherm could be categorized as IV-type with a distinctive hysteresis loop, referred to as the formation of pores in the mesoscale (2–50 nm pore size). The Brunauer–Emmett–Teller (B.E.T.) for MWSS surface area is 79 $m^2/g$ with a pore volume of 0.356 $cm^3/g$. Based on the gained data, the pore size of MWSS is about 8.6 and 5.84 nm according to the Barrett–Joyner–Halenda (BJH) method and the density functional theory (DFT) methods, respectively. This unique structure of mesoporous MWSS can provide a great feature for the employed material for MB-adsorption and photocatalytic degradation.

To investigate the functionality of the MWSS, the MWSS sample was characterized using FTIR spectroscopy. The produced FTIR spectrum in Figure 2b indicated several absorption bands mainly associated with the straw-derived $SiO_2$ platform. The broad peak at around 3447 $cm^{-1}$ is assigned to the stretching (-OH) vibration of silanol (Si-OH), Ni-OH, and Co-OH in the MWSS, and it could be assigned to the trapped water molecules on the surface of the MWSS. A small peak was noticed at 1635 $cm^{-1}$ in the IR spectrum, representing the bending vibration of the trapped $H_2O$ molecules in the MWSS matrix. The three absorption bands at 1087, 799, and 460 $cm^{-1}$ are recognized to three different vibration modes for the Si-O-Si bond in the structural framework as follows: asymmetric stretching, symmetric stretching, and bending vibrations, respectively. Moreover, the peaks between 1000 and 400 $cm^{-1}$ may be assigned to the Ni-O-Ni and Co-O-Co vibrations (Itteboina and Sau 2019; Mezan et al. 2021; Sharma et al. 2021).

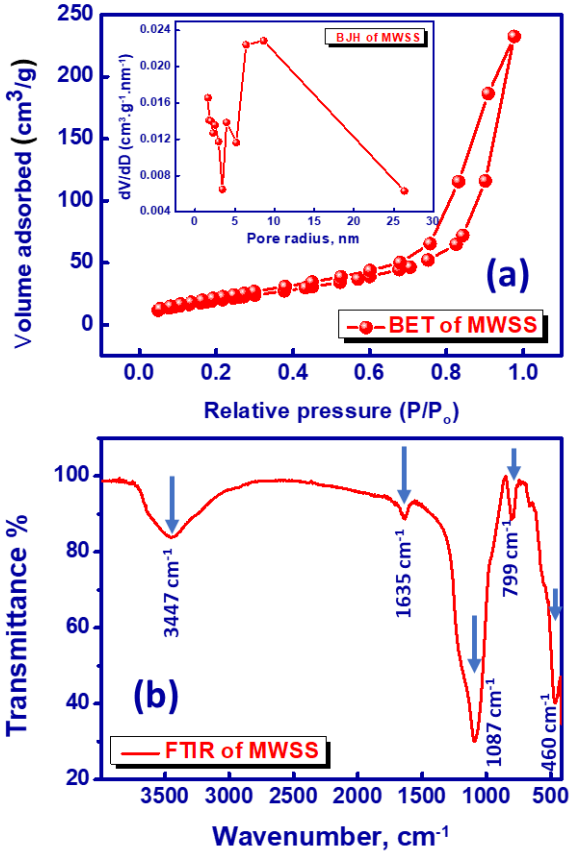


222

223 **Figure 2.** (a) $N_2$ adsorption-desorption isotherm and BJH of mesoporous MWSS, and (b) FTIR of

224 mesoporous MWSS.

225

226 SEM analysis was employed to achieve evidence on the structure of the prepared MWSS

227 material, as shown in Figure 3a-e. The top-view SEM images of MWSS powder explain that

228 the MWSS was prepared in a spongy structure. This spongy morphological can be shown even

229 better at a larger enlargement scale. Figure 3a&b shows the micro-sized grains of MWSS-like

230 rock containing nano-holes and grooves with a size less than 100 nm, the distribution of nano-

231 holes along the micro-grains is relatively uniform. The spongy structure offers a large surface

232 area and consequently excellent characteristics as an adsorbent or photocatalyst material due

233 to the growth of surface-active sites. Moreover, the spongy shape leads to facilitates the

234 diffusion of MB-molecules within the MWSS material. Furthermore, the chemical composition

of MWSS has been validated via the qualitative and quantitative EDX analysis, as shown in Figure 3f. The obtained EDX analysis data indicated that the atomic percentage % of MWSS components were 58.66, 29.33, 6.25, and 5.75 % for oxygen, silicon, nickel, and cobalt elements, respectively. These findings suggest the strong composition of Ni-Co oxides inside the internal matrix of the wheat straw-derived silica scaffold.

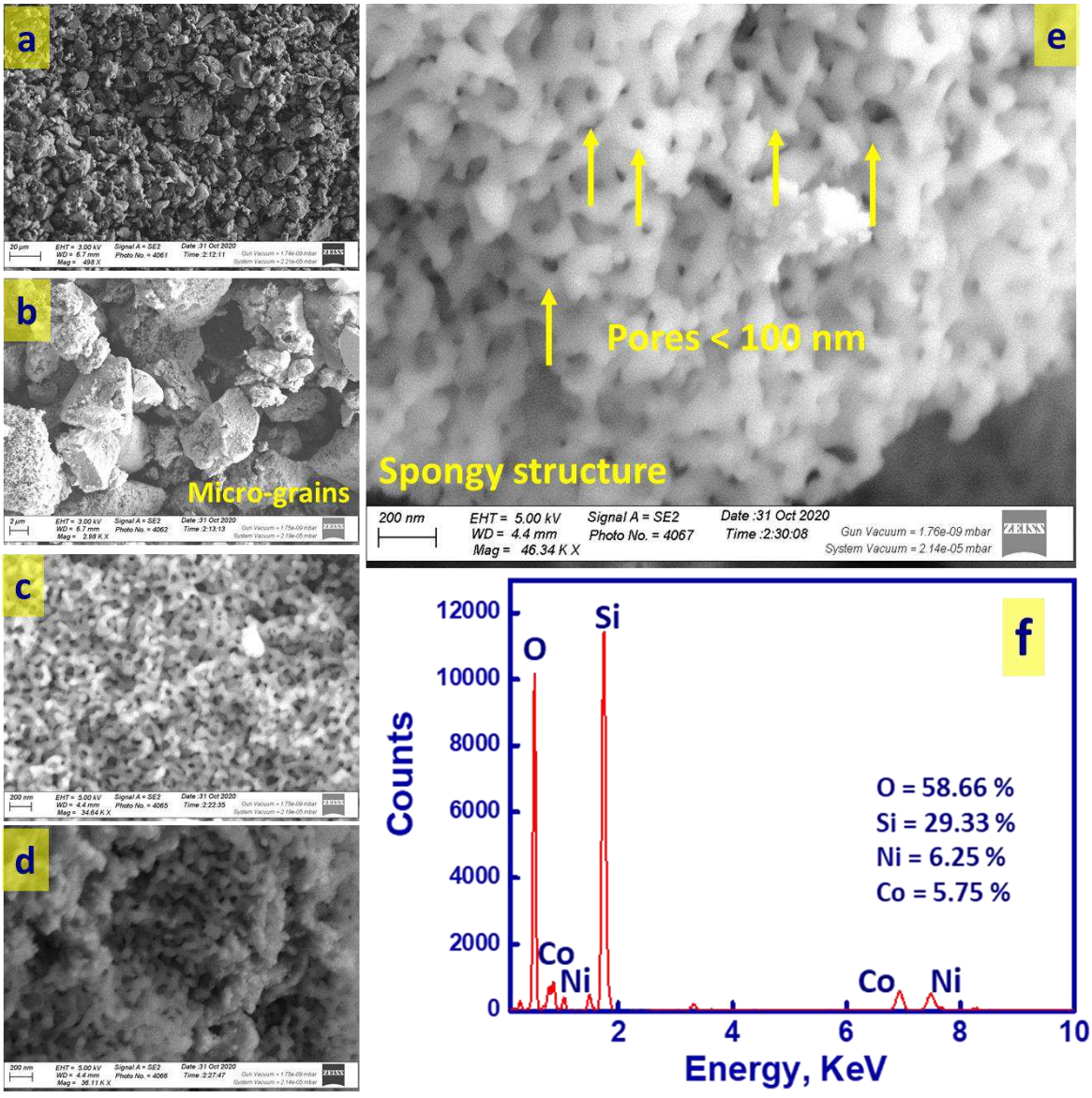

**Figure 3.** (a-e) Top-view S.E.M. images of mesoporous spongy MWSS, and (f) SEM-EDX profile of mesoporous spongy MWSS.

Furthermore, thermogravimetric analysis (TGA) and Differential thermal analysis (DTA), as displayed in Figure 4, have been applied to assess the thermal stability of the MWSS. From the TGA thermograms, the TGA curve of MWSS shows two clear thermal degradation steps as follows: (i) a small weight lack, about 4%, has been detected in the temperature scale 21 $^{o}$C to 151 $^{o}$C, due to the physically absorbed $H_2O$ during synthesis process and from moisture during sample storing; and (ii) about 3.2% was lost in the temperature range 154 $^{o}$C to 593 $^{o}$C, due to the decomposition and pyrolysis of MWSS framework. While, the DTA curve shows the differential temperature change in the range of 21: 151 $^{o}$C and displays an exthothermic peak at around 87°C, which is attributed to the same reason above and increases the crystallinity of the mesoporous spongy MWSS as well. However, no evidence of endothermic peaks was found in the whole range of temperature, which predicted no sign of decomposition or any phase transation of MWSS under thermal stress. The acquired data suggested the strong thermal stability of our mesoporous MWSS structure even at high temperatures up to 600 °C.

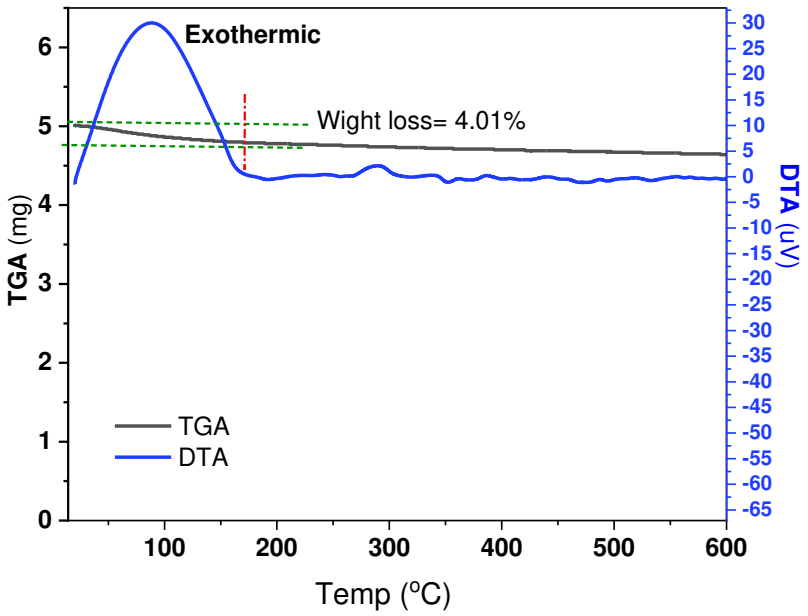


**Figure 4.** Thermal analysis of both TGA and DTA for mesoporous MWSS.

### 3.2.Influence of pH on the MB-adsorption and photodegradation mechanism

pH is deemed as a highly vital key factor controlling MB-adsorption and photodegradation. The pH value strongly contributes to changing the outer surface active site charge type, resulting in either the development or decline of MB-adsorption and photodegradation efficiency. Therefore, the influence of pH value on the MB-adsorption and photocatalytic degradation using MWSS was explored to determine the optimum pH condition under the experimental conditions (MWSS dose: 50 mg; solution volume: 50 mL; contact time: 60 min; MB-concentration: 5 ppm; at a wide pH range: pH 2- pH10) through a series of benchtop-batch tests. As shown in Figure 5a, the maximum MB-adsorption and photodegradation efficiency was achieved at pH 10, where the MB-removal efficiencies were 79 and 93 % through adsorption and photodegradation processes, respectively. The obtained findings indicated that the MB-removal using MWSS is strongly conditional on the pH value of MB-solution. Figure 5b shows the zeta potential profile of MWSS at different pH values to evaluate the surface

charge of MWSS material. The point of zero charge (i.e., the pH value at which the surface charge is zero, pzc) was at pH 5.3. At a high acidity level (pH < 5.3), the outer surface-active sites charge of MWSS is positive, leading to a decrease in the MB-adsorption and photodegradation efficiency, where MB is a positively charged cationic dye. Furthermore, the competition of $H_3O^+$ ions at the active sites of the MWSS-surface was also led to reducing the efficiency of MB-adsorption and photodegradation. With increasing pH values (i.e., pH > 5.3), the MB-adsorption and photodegradation efficiency was improved because the MWSS surface-active sites were starting to be charged negatively, agreeing to the zeta potential values, and the competition between the positively MB-molecules and $H_3O^+$ ions was reduced (see Scheme 2).

On the other hand, enhancement of MB-adsorption leads to improvement in the photocatalytic degradation process. MB-molecules reach many active sites to degrade methylene blue under UV-irradiation. Under UV-irradiation, energy generates the electron ($e^-$) and positive electron-hole ($h^+$) pairs onto the MWSS surface, leading to reduction-oxidation reactions. The excitation of electrons from the valence band (VB) to the conduction band (CB) of the MWSS generates an $h^+_{VB}$ in the VB when the energy of the UV-light goes above the bandgap energy value of the MWSS. The accurate bandgap energy value of the NiO&$Co_2O_3$ and MWSS was established using the Tauc relationship as follows (Rani et al. 2018):

$$(\alpha h\nu)^2 = A\left(h\nu - E_g\right) \quad (3)$$

Where α, A, h, ν, and Eg are the absorption coefficient, constant, Plank's constant, frequency, and bandgap energy. The curve of $(\alpha h\nu)^2$ against photon energy shows an intermediary linear zone. The Tauc's zone was referred to bandgap energies of 2.77 and 3.2 eV for NiO&$Co_2O_3$ mixture and MWSS, respectively (see Figure 5c&d), which indicates that MWSS can be deemed as a good photocatalyst to decompose MB contaminants. In the case of MWSS, the

bandgap is a little bit larger than that of the NiO&$Co_2O_3$ mixture due to the formation of the composite structure with wheat straw-derived $SiO_2$. As explained in the following equations, the holes ($h^+_{VB}$) were trapped by $H_2O$ on the surface of MWSS to generate $H^+$ and •OH radicals, which was an efficient oxidizing agent to degrade MB-molecules to $CO_2$ and $H_2O$. The •OH radicals have been the vital effective species during the MB-photocatalytic process. At pH 10, the MB-dye was then switched to a cationic species, contributing to the MB-degradation. Besides, the $e^-_{CB}$ captured $O_2$ to produce anionic superoxide ($O_2^{-\bullet}$) radical. The reaction of $H^+$ of $O_2^{-\bullet}$ leads to form hydroperoxy radical, then converted into $H_2O_2$. The formed $H_2O_2$ can be dissociated into 2•OH radicals responsible for the degradation of MB-molecules (see Scheme 1) (Atout et al. 2017). At high pH conditions (i.e., pH 10), increasing $OH^-$ concentration may lead to enhance the photodegradation efficiency, where $OH^-$ can be reacted with $h^+$ to form many of the •OH radicals and $H^+$ ions, explaining the decrease of solution-pH at the end of the photocatalytic degradation process.

$$\text{MWSS} + h\upsilon \rightarrow (e^-_{CB} + h^+_{VB})@\text{MWSS}$$

$$MB + \text{MWSS} \rightarrow \text{MB}^{\cdot+} + e^-_{CB}\ (\text{MWSS})$$

$$H_2O + h^+_{VB} \rightarrow HO^{\cdot} + H^+$$

$$O_2 + e^-_{CB} \rightarrow O_2^{-\cdot}$$

$$O_2^{-\cdot} + H^+ \rightarrow HOO^{\cdot}$$

$$2HOO^{\cdot} \rightarrow H_2O_2 + O_2$$

$$H_2O_2 \rightarrow 2HO^{\cdot}$$

$$\text{MB}^{\cdot+} + OH^{\cdot} \rightarrow CO_2 + H_2O + other\ products$$

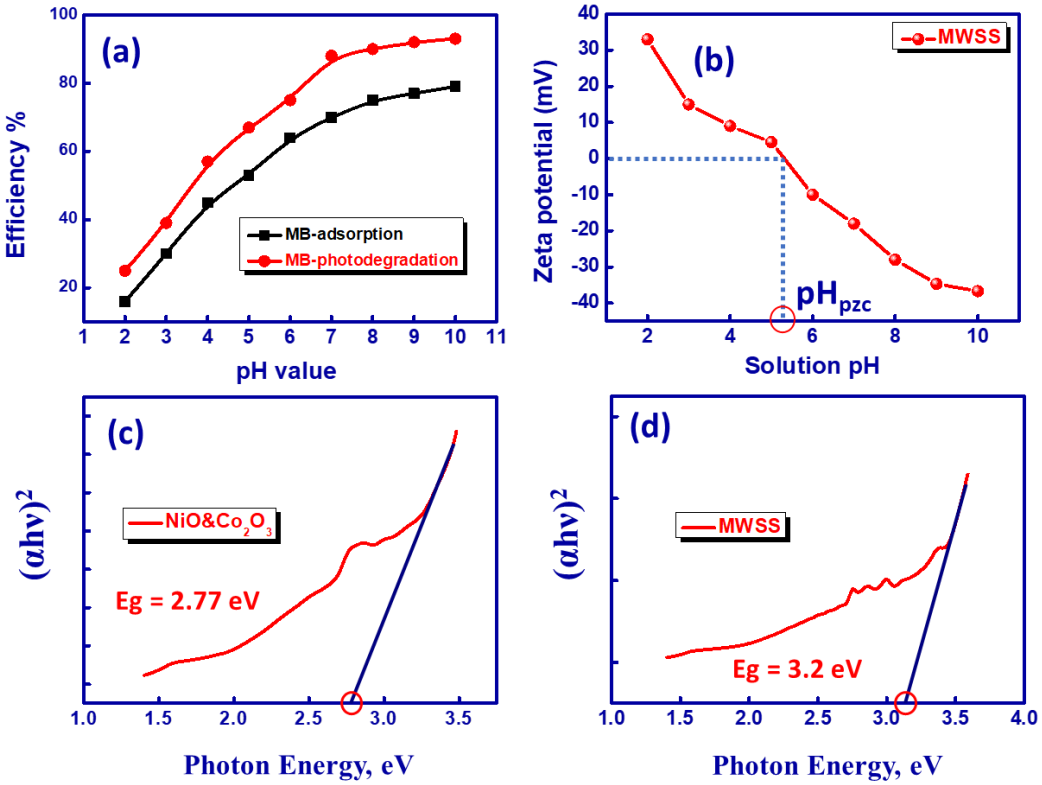


320

321 **Figure 5**. (a) Influence of pH on the MB-adsorption and photodegradation using mesoporous MWSS,
322 (b) Zeta potential of MWSS to evaluate the charge of the surface at various pH values (pH 1.0 – 10.0),
323 (c and d) the plot of (αhυ)2 against hν (eV) of the NiO&$Co_2O_3$ composite and mesoporous MWSS
324 samples to calculate the Eg using Tauc equation.

325

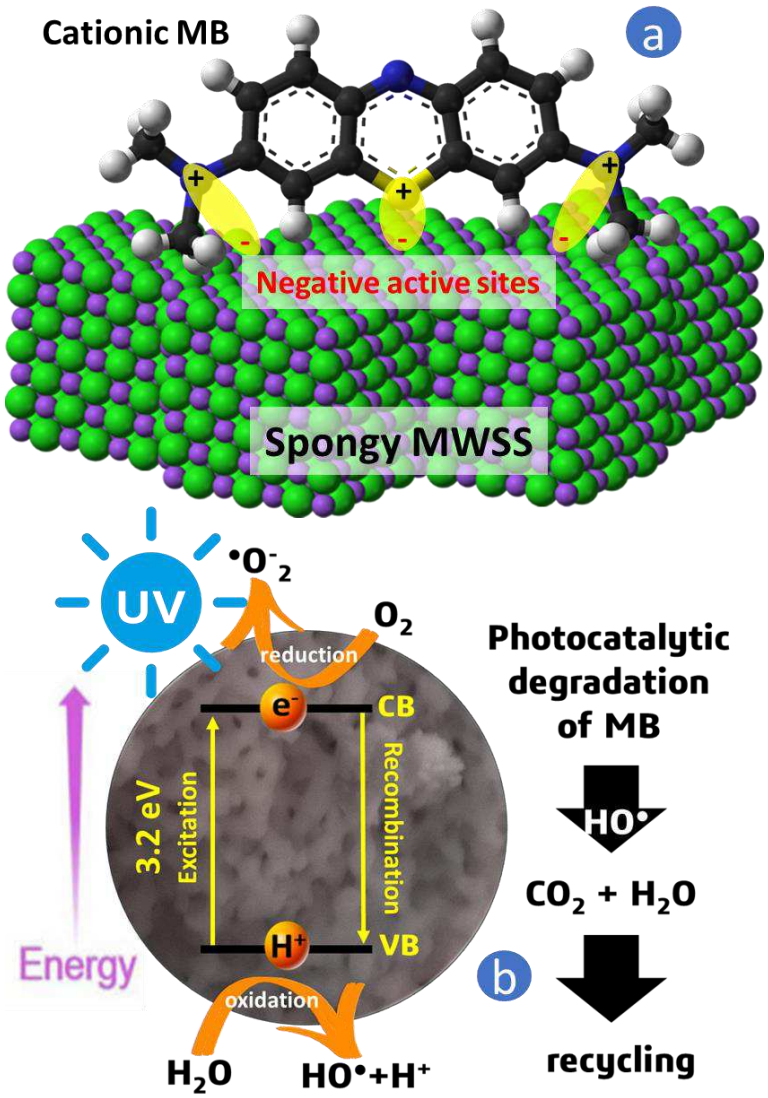


326

327 **Scheme 2.** Schematic design shows (a) the MB-adsorption and (b) the MB-photocatalytic degradation

328 mechanism using mesoporous spongy MWSS adsorbent/photocatalyst.

329

330

331

332 **3.3.Effect of dosage, time, temperature, and MB-concentration on the MB-**

333 **adsorption and photodegradation process**

In the photocatalytic degradation reaction, the performing of the MWSS is mainly defined by three assets: the adsorption of MB, the light penetration to the surface-active sites, and the transport of photogenerated radicals. Therefore, various physicochemical factors such as the MWSS dosage, contact time, temperature, and initial MB-concentration were verified to assess the MB-adsorption and photodegradation process. The amount of MWSS is a vital factor influencing the MB-adsorption and photodegradation process significantly. Therefore, the impact of MWSS dosage on the MB-adsorption and photodegradation efficiency was explored under optimal pH circumstances using various doses of MWSS (10 mg to 150 mg) to determine the amount of the MWSS required to remove the maximum amount of MB during the process. The obtained results in Figure 6a indicated that the quantity of MB-dye removed by the samples was discovered to expand upon growing the quantity of MWSS due to the availability of more surface-active sites for the MB-adsorption and photodegradation. At a low dose, the MB-adsorption and photodegradation rate was decreased due to the reduction of electron−hole pairs formation rate, and thus fewer hydroxyl radicals are formed.

Moreover, batch trials were done to survey the impact of time on the MB-adsorption and photodegradation performance. Figure 6b exhibits that MB-adsorption and photodegradation efficiency gradually increased with the increasing reaction time until equilibrium was achieved. The fast removal of MB-dye within 20 min was due to the availability of vacant active sites, which allowed the MB-molecules to interact readily at the MWSS surface. This implies that the prepared MWSS has good adsorption and photocatalytic activity for MB is likely to be an efficient adsorbent and photocatalyst. Also, Figure 6c reveals that the MB-adsorption and photodegradation efficiency increased with the rising temperature of the adsorption and photodegradation vessel process from 25 to 60±2$^{o}$C. These findings proved that the MB-removal is an endothermic procedure. High temperature accelerates the adsorption and photodegradation rate and improves the diffusion of MB-molecules between the bulk solution

and adsorbent/photocatalyst surface. Lastly, the impact of initial MB-concentration on the adsorption and degradation of MB-dye using MWSS was also assessed. As demonstrated in Figure 6d&e, the MB-adsorption and photodegradation efficacies were discovered to differ significantly while the initial MB-concentration is changed. The MB-adsorption and photodegradation efficacies declined when the concentration of MB expanded. Figure 6d exhibited that the maximum MB-adsorption is about 44 mg per 1 gram of MWSS adsorbent. Moreover, the expansion of MB-molecules along the surface-active sites may inhibit the diffusion of UV-light to the MWSS outer surface, leading to a decrease of $^{\bullet}OH$ radicals' generation, slowing the MB-photodegradation kinetic rate, and hence reduce of MB-photodegradation efficiency. This behavior can be caused by the MB-degradation process's intermediate products, which would compete with MB for reaction with $^{\bullet}OH$ radicals. At higher initial MB-concentration, the intermediates' concentrations are also higher.

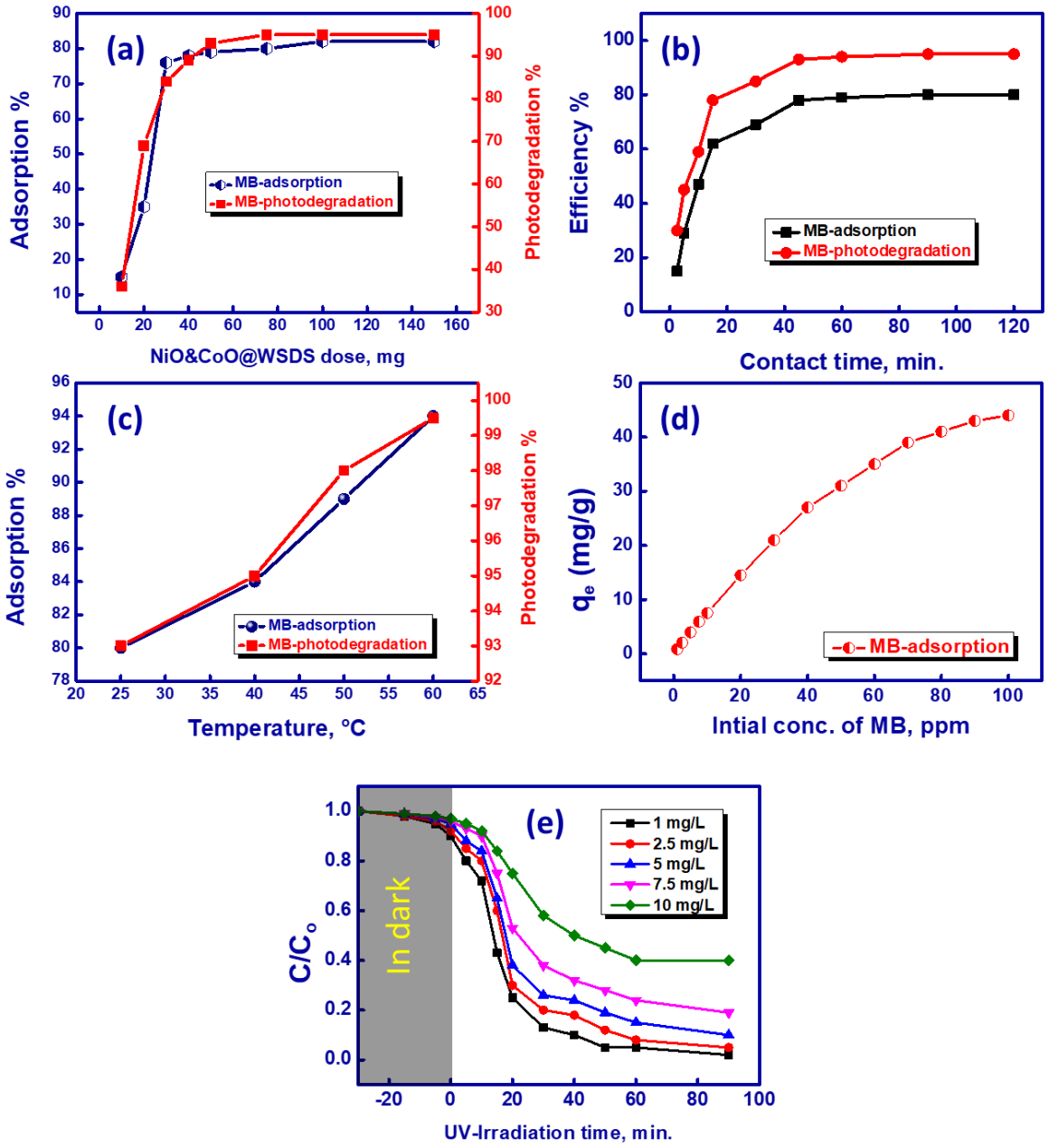


372

373 **Figure 6.** Effect of MWSS dosage (a), contact time (b), temperature (c), initial MB-concentration (d

374 and e) on the MB-adsorption and photodegradation.

375

376 **3.4.Molecular dynamics (MD) calculations**

377 MWSS (001) surfaces have been chosen to compare methylene blue (74-molecule) binding

378 behavior and the typical favorable nature of (001) face noted in the well-shaped crystals.

However, the Si atoms (top surface) were surrounded by four oxygen. To study the effect of NiO and $Co_2O_3$ at the interface of MWSS, the Si atoms (top surface) were modified by (Si 70.96%, Ni 15.12%, Co 13.91%) based on the experimental ratio out of EDX analysis. MD has been used to examine the capacity of Ni/Co oxides to modify the surface of MWSS toward adsorption of methylene blue. Figure 7a shows the optimized layers of MWSS (001) surfaces and methylene blue molecules under the MD restrictions in Figure 7b. However, the top surface disruption (Figure 8) was notable due to dynamic interaction attributed to the penetration of methylene blue molecules into the outer layer of MWSS (001) surfaces by Ni and Co oxides.

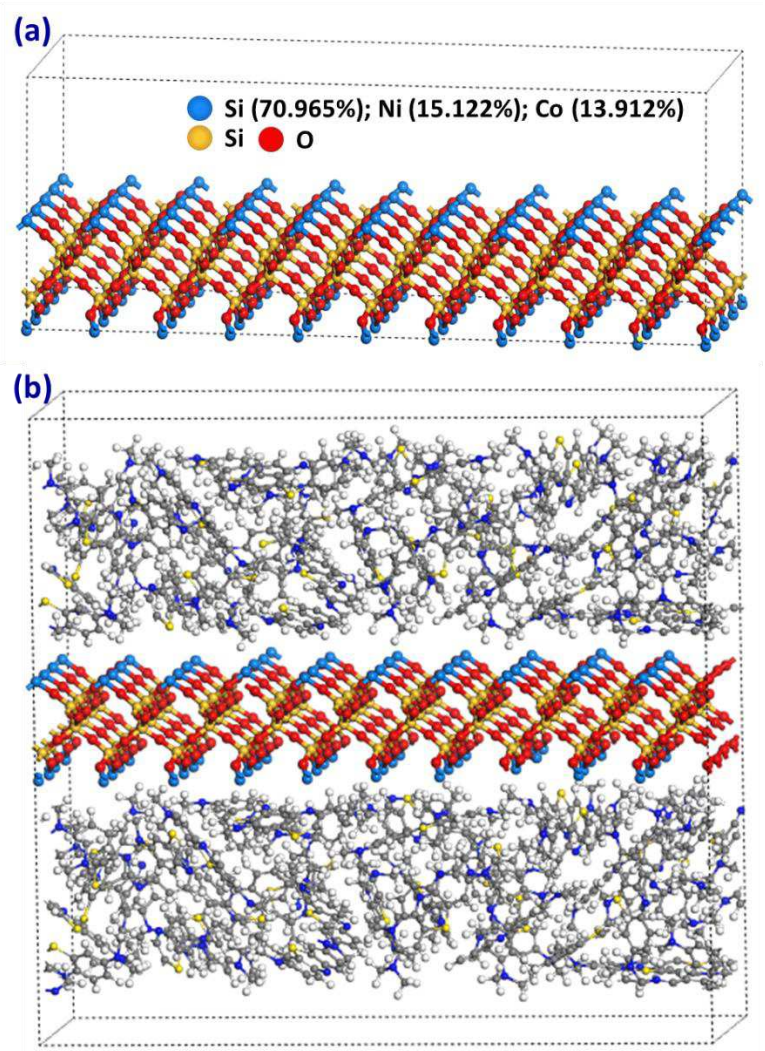


**Figure 7.** Representative Ni/Co oxides @ MWSS (a); and binding conformations methylene blue on Ni/Co oxides @ MWSS (001) surface.

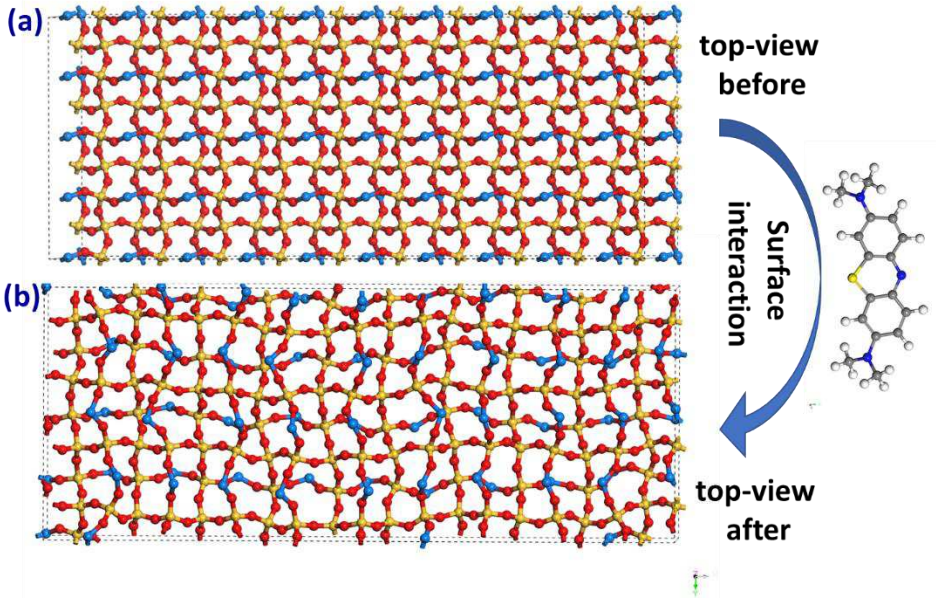


**Figure 8.** Top view of Ni/Co@ MWSS before (a); and after (b) molecular dynamics of methylene blue on (001) surface.

It worth mentioning, the unmodified WSS has less interaction than MWSS toward methylene blue molecules, as shown in Figure 9a. The concentration profiles and the small distance between and MWSS and methylene blue camper to unmodified WSS resulting from molecular dynamics simulation predict the role of Ni and Co atoms in the top surface toward the adsorption behaviors, as we confirmed by experimental results. In particular, the distance of each atom between MWSS and methylene blue shows that the O atoms of MWSS was close enough to attract mainly to the S and H atoms of methylene blue by electrostatic bonds and hydrogen bonding as well (Figure 9b). Optimized total energies of methylene blue, WSS, MWSS and the layers interaction of MB on both modified/nonmodified WSS (001) surfaces were collected in Table 1. The individual binding energy of WSS (ca. −13862.28 kcal/mol) almost similar to the MWSS (ca. −13862.28 kcal/mol) calculated by Forcite module using of

force field COMPASS II. However, the binding energy of MB@ MWSS (ca. -2154.91 kcal/mol) was much better than the nonmodified surface of WSS (ca. -2138.54 kcal/mol), which is in accordance with experimental observations.

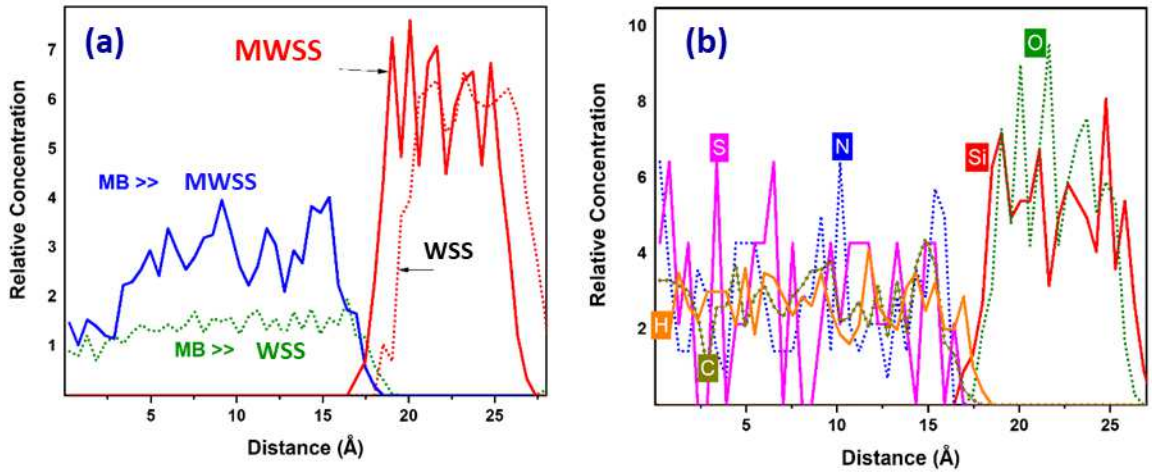


**Figure 9.** Concentration profiles of methylene blue with and without Ni/Co top surface of WSS (a); atoms in MWSS and methylene blue are displayed for (001) systems.

**Table 1.** Total energies (kcal/mol) of methylene blue (MB), WSS, MWSS, and MB layer interaction on the WSS and MWSS surfaces.

| | MB | WSS | MWSS | MB@WSS | MB@ MWSS |
|---|---|---|---|---|---|
| Total energy | 432.657 | -13862.28 | -13862.31 | -15568.16 | -15584.56 |

### 3.5.MB-adsorption isotherm investigations

MB-adsorption isotherm offers info concerning the type of interactions between MB-dye and MWSS as an adsorbent with different initial MB-concentrations under the optimum MB-adsorption circumstances. The relationship between equilibrium MB-concentration ($C_e$) in the solution and the adsorption capacity ($q_e$) of MWSS adsorbent can be obtained with different adsorption isotherm prototypes. To identify the MB-adsorption mechanism, Langmuir and Freundlich's models were studied (Seera et al. 2021). According to the Langmuir isotherm model, the MB-molecules adsorb on the MWSS adsorbent's surface and thus produce a monolayer of MB-molecules on the MWSS surface-active sites through real chemical bonds. On the other hand, the Freundlich adsorption isotherm model suggests forming a multilayer of MB-molecules onto the MWSS surface through physical attraction forces. The linearized form of the Langmuir and Freundlich isotherm models are given by the following equations (Gomaa et al. 2018):

$$\frac{C_e}{q_e} = \frac{1}{K_L q_m} + \left(\frac{1}{q_m}\right) C_e \qquad (4)$$

$$R_L = {}^{1}/_{(1 + K_L C_o)} \qquad (5)$$

$$\ln q_e = \ln K_f + \frac{1}{n} \ln C_e \qquad (6)$$

$q_m$, $K_L$, and $C_o$ are the theoretical MB-adsorption capability of MWSS (mg/g), constant of the MB-adsorption equilibrium, and initial MB-concentration, respectively; $K_F$ and n are the proportional adsorption capacity of MWSS and adsorption strength, respectively. n value indicates the favourability of MB-adsorption. All these constants are defined from the slope and intercept of the linear relations of $C_e/q_e$ versus $C_e$ and $\ln q_e$ versus $\ln C_e$ plots (see Figure 10a&b and Table 2). By judging the correlation coefficients ($R^2$) values, the obtained results were best attached for the Langmuir isotherm model, with an $R^2$ value of 0.992. This suggested the MB-adsorption mechanism onto MWSS was a monolayer and chemically adsorption process. According to the data achieved from the Langmuir isotherm model, the maximum MB-adsorption

capacity onto MWSS was 55.5 mg/g, this value is relatively close to the experimental value. Furthermore, the $R_L$ value of MWSS was lower than 1, signifying the MB-adsorption process was favorable and fully reversible. This outcome indicates that the adsorbed MB-dye can be released from the MWSS adsorbent surface during the chemical regeneration treatment. The n value is between 1 and 2, so the MB-adsorption process is considered moderate or relatively hard adsorption. The mesopore facilitated the diffusion of MB-molecules within MWSS adsorbent, suggesting that MWSS was a promising candidate adsorbent for MB pollutants.

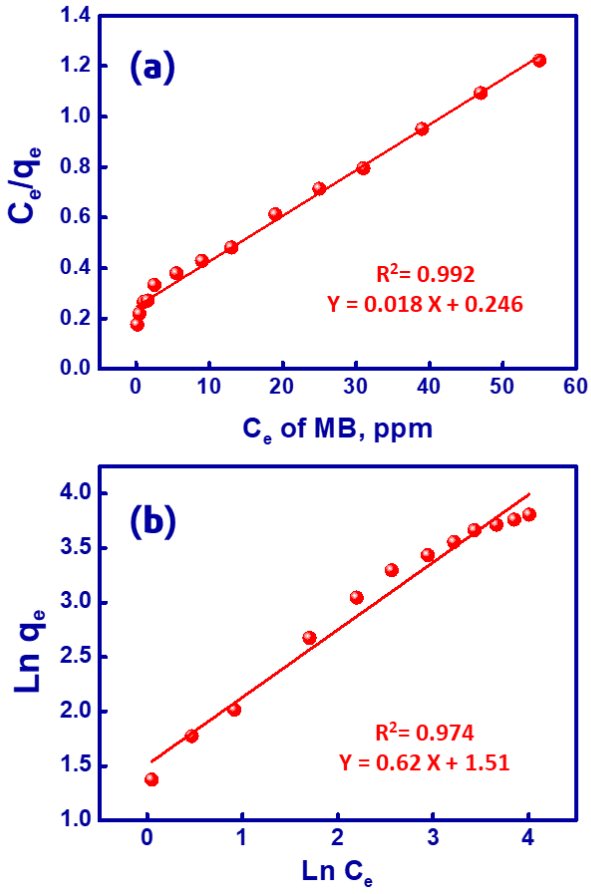


**Figure 10.** Isotherm study of MB-adsorption by Langmuir (a) and Freundlich (b) adsorption isotherm versions using mesoporous MWSS adsorbent.

**Table 2.** Parameters of Langmuir and Freundlich isotherm models for the MB-adsorption using mesoporous MWSS adsorbent.

| | | | | |
|---|---|---|---|---|
| **Langmuir** | $R^2$ | $q_m$ mg/g | $K_L$ L/mg | $R_L$ |
| | 0.992 | 55.5 | 0.073 | < 1 |
| **Freundlich** | $R^2$ | n | $K_F$ L/mg | |
| | 0.974 | 1.6 | 4.52 | |

### 3.6.MB-decolorization kinetic studies

To study the mechanism of MB-adsorption and potential rate-controlling steps under the optimum MB-adsorption conditions, two commonly accepted kinetic models (the pseudo 1st and 2nd order models) were applied to fitting the present investigational results, which are as follows, where the adsorption kinetics was investigated at variable times from 1 to 60 min (Gomaa et al. 2021):

$$log(q_e - q_t) = log\, q_e - \left(\frac{K_1}{2.303}\right) t \quad (7)$$

$$\frac{t}{q_t} = \frac{1}{K_2 q_e^2} + \left(\frac{1}{q_e}\right) t \quad (8)$$

$K_1$ and $K_2$ are the rate constants of the pseudo 1st (min-1) and 2nd (g/mg.min) order models. $q_e$ and $q_t$ are the MB-adsorbed quantities (mg/g) at equilibrium and time t, respectively. These corresponding model fitting parameters were calculated from the slope and intercept by plotting Log($q_e$-$q_t$) and t/$q_t$ against time and then summarized in Table 3. According to $R^2$ values in Figure 11a, the adsorption of MB-dye followed the pseudo 2nd order model, referring to that the MB-sorption mechanism using MWSS is chemisorption. The MB-removal was relatively rapid at the initial step of the adsorption process and slowed down before achieving

476 the equilibrium point. The calculated $q_e$ value of the pseudo 2$^{nd}$ order model was like the
477 experimental $q_e$ value when the initial MB-concentration was 5 ppm.

478 The kinetic rate of the MB-photocatalytic degradation using MWSS photocatalyst can be
479 determined from the following equations' 1st and 2nd order linear models. According to the
480 apparent 1$^{st}$ and 2$^{nd}$ kinetics formula, $C_o$ is the initial MB-concentration, and $C_t$ is the final MB-
481 concentration after time t (Rahman and Kar 2020):

482 $$ln\frac{C_o}{C_t} = K_1 \times t \qquad (9)$$

483 $$\frac{1}{C_t} = K_2 \times t \qquad (10)$$

484 The calculated values of rate constant ($K_1$ and $K_2$) of pseudo 1$^{st}$ and 2$^{nd}$ order models, half
485 lifetime ($t_{0.5}$), and $R^2$ are shown in Table 3. The $t_{0.5}$ (min.) can be determined through ($0.693/K_1$)
486 and ($1/K_2C_o$) equations for pseudo 1$^{st}$ and 2$^{nd}$ orders, respectively. A linear relationship of
487 $\ln(Co/C_t)$ and $1/C_t$ versus the time intervals (t) is shown in Figure 11b. From the values of $R^2$,
488 the MB-photocatalytic degradation followed the pseudo 1$^{st}$ order model. Under UV irradiation,
489 the shift of mechanism from pseudo 2$^{nd}$ order kinetics for adsorption to pseudo 1$^{st}$ order kinetic
490 indicates that MB-photocatalytic degradation is a physical process. Therefore, to complete MB-
491 removal through the photocatalytic degradation approach, firstly, MB-molecules should be
492 adsorbed on the MWSS surface.

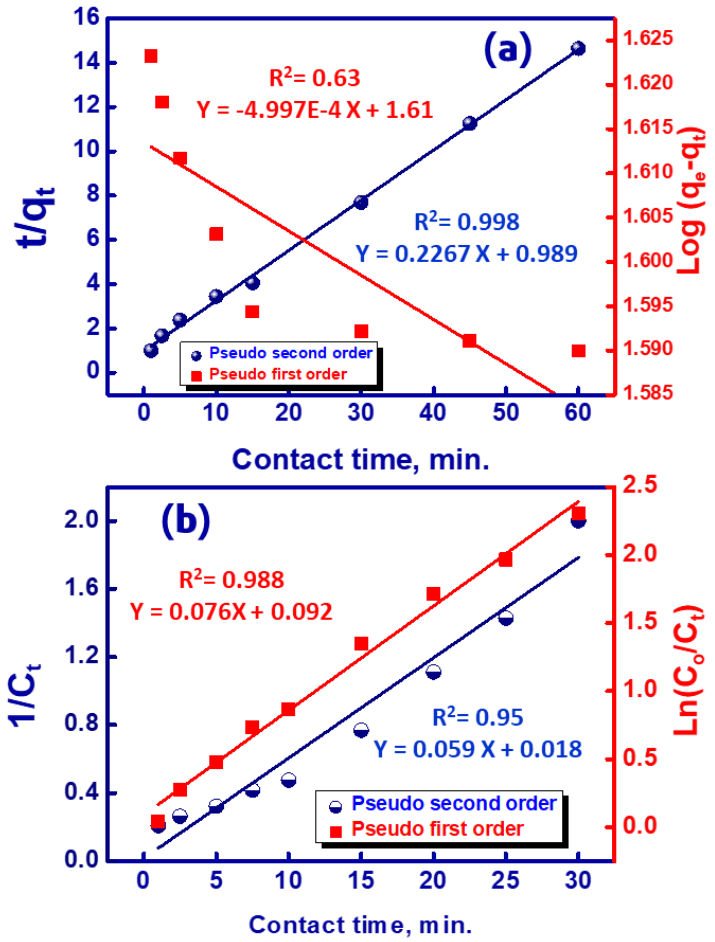


493

494 **Figure 11.** Kinetic study of MB-adsorption (a) and MB-photocatalytic degradation (b) using
495 mesoporous MWSS adsorbent/photocatalyst through pseudo 1st and 2nd order kinetic models.

496

497

498 **Table 3.** Parameters of pseudo 1st and 2nd order kinetic models for the MB-adsorption and photocatalytic
499 degradation using mesoporous MWSS adsorbent/photocatalyst.

| | **Pseudo-first-order** | | | **Pseudo-second-order** | | |
|---|---|---|---|---|---|---|
| **Adsorption** | $R^2$ | $K_1$ 1/min | $q_e$ mg/g | $R^2$ | $K_2$ g/mg.min | $q_e$ mg/g |
| | 0.63 | 0.00115 | 40.7 | 0.998 | 0.052 | 4.4 |
| | $R^2$ | $K_1$ | $t_{0.5}$ | $R^2$ | $K_2$ | $t_{0.5}$ |

| | | | | | | |
|---|---|---|---|---|---|---|
| **Photodegradation** | 0.988 | 0.076 | 9.11 | 0.95 | 0.059 | 3.39 |

### 3.7.Regeneration and reusing of MWSS

The reusability of the MWSS adsorbent/catalyst under repeated reuse cycles encompasses an essential perspective in the lab and scale-up applications. The adsorption and photocatalytic degradation processes are also the most economical methods for MB-removal from wastewater, because of the reproducibility enable of spent adsorbent or photocatalyst materials. The elution process permits using the spent adsorbent/photocatalyst several times to minimize the overall MB-removal cost. The adsorption of MB-dye at the inner/outer active sites of mesoporous MWSS adsorbent/catalyst, whether adsorption or photodegradation process, may reduce inner/outer active sites leading to decrease the MB-adsorption and photodegradation efficiency. Therefore, these experiments aim to evaluate how to efficiently reuse the MWSS adsorbent/catalyst for long-term utilization. A set of batch-tests were done to study the impact of $HNO_3$ concentration and elution time on the MB-elution effectiveness. The regenerated MB-free MWSS solid was filtered, dried, and used for further treatments, displaying its reusability. The elution % of adsorbed MB-dye from MWSS solid was determined as follows: Releasing or elution $\% = (C_R/C_A)$ x100, where $C_R$ and $C_A$ are the released and adsorbed MB-concentration in ppm, respectively.

As indicated in Figure 12a, MB-elution % was enhanced with expanded $HNO_3$ concentration and contact time. The finding data revealed that >99 % of adsorbed MB-dye could be released using 1 M $HNO_3$ under stirring for 30 min. As illustrated in Figure 12b, the regenerated MWSS remains highly effective and can be employed for numerous reuse/cycles. After each cycle, the MB-removal efficiency was slightly reduced. After the $5^{th}$ cycle ($1^{st}$ round of MWSS cycling), the MB-removal efficiency was 65% and 77% through the adsorption and photodegradation

process, respectively (see Figure 12b). To investigate the dead-end usage of MWSS recycling, the 5-cycle regenerated MWSS (after 1st round cycling) surfaces were re-activated via calcination at 500°C for 4 h, to be ready for the 2nd round of MB-removal (i.e., for further 5 reuse/cycles), as shown in Figure 12c. This study will open a new route to MB-removal from real wastewater efficiently with low cost. After a further 5 reuse/cycles, the MB-removal efficiencies were 60%, and 72% through adsorption and photodegradation processes, respectively. The decrease of the adsorption and photodegradation efficiency may be due to the potential influence of the eluent $HNO_3$ on the reused-MWSS surface-active sites. Therefore, the obtained data show the probability of using MWSS adsorbent/catalyst numerous times in MB-removal from wastewater.

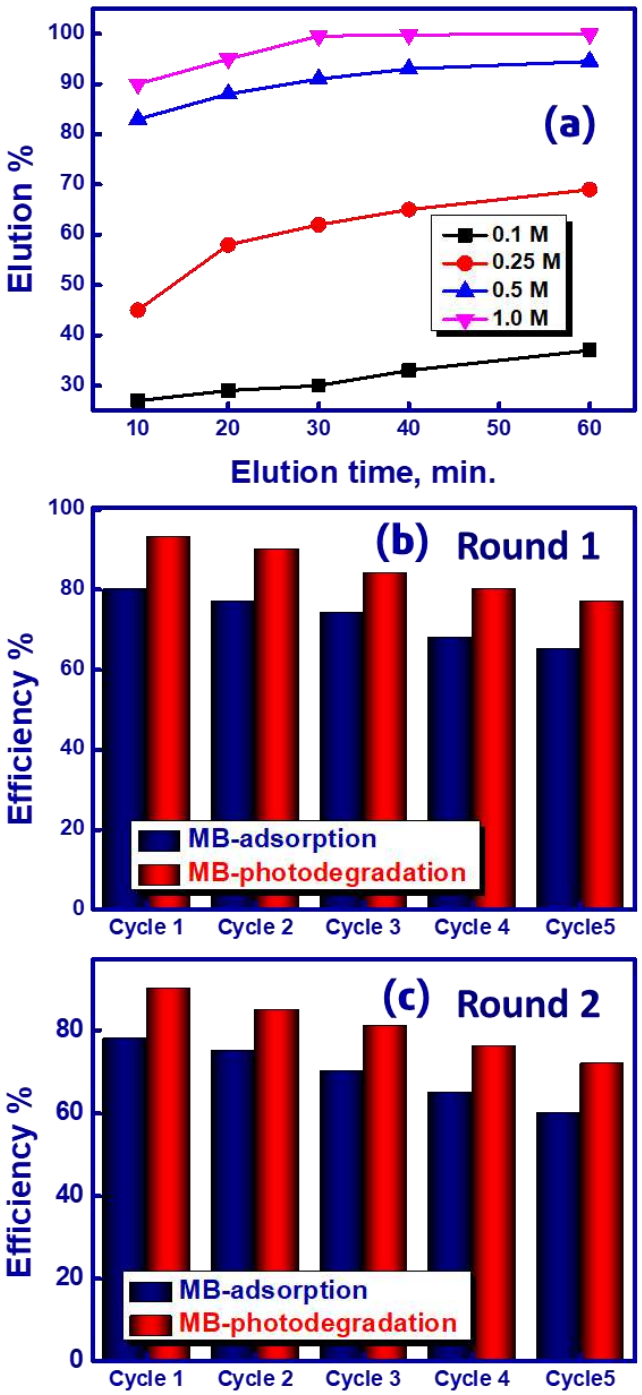


533

534 **Figure 12.** (a) Impact of $HNO_3$ concentration and contact time on the regeneration efficiency of MWSS

535 adsorbent/photocatalyst, (b and c) first and second round of spent mesoporous MWSS recycling

536 as a function of MB-adsorption and photodegradation efficiency.

537

## 4. Conclusion:

The novel mesoporous spongy MWSS adsorbent/photocatalyst was successfully designed for MB-decolorization through adsorption and photocatalytic degradation approaches. Our findings indicated that about 80 and 93% of cationic MB-dye could be removed at pH 10. The MB-adsorption followed Langmuir isotherm, and pseudo 2$^{nd}$ order model, while the MB-photodegradation followed the pseudo 1$^{st}$ order model. The larger surface area and mesoporosity led to a maximum adsorption capacity of 44 mg/g and fast diffusion of MB along the MWSS adsorbent/photocatalyst surface. Moreover, the mesoporous MWSS adsorbent/photocatalyst can be recycled for ten reuse cycles, a potential nominee for adsorption and photocatalytic degradation of MB-dye. Therefore, the MWSS adsorbent/photocatalyst with high adsorption and photodegradation efficiency would be a promising adsorbent or photocatalyst for the MB-removal from wastewater.

**Ethical Approval:** Not applicable

**Consent to Participate:** Not applicable

**Consent to Publish:** Not applicable

**Authors Contributions:**

Conceptualization: [H. Gomaa]; Methodology: [Mohamed A. T. Hussein, Mohamed M. Motawea]; Formal analysis and investigation: [Mohamed M. Elsenety]; Writing - original draft preparation: [All authors]; Writing - review and editing: [All authors]; Funding acquisition: [Salah M. El-Bahy]; Supervision: [H. Gomaa]. All authors read and approved the final manuscript.

**Funding**

The authors gratefully acknowledge financial support from Taif University Researchers Supporting Project number (TURSP-2020/135), Taif University, Taif, Saudi Arabia.

**Competing Interests:** The authors declare that they have no competing interests

**Availability of data and materials:** Not applicable

**References:**


Abdelwahab AA, Naggar AH, Abdelmotaleb M, Emran MY (2020) Ruthenium Nanoparticles Uniformly-designed Chemically Treated Graphene Oxide Nanosheets for Simultaneous Voltammetric Determination of Dopamine and Acetaminophen. Electroanalysis 32:2156–2165. https://doi.org/https://doi.org/10.1002/elan.202060126

Abdien HG, Cheira MF, Abd-Elraheem MA, et al (2016) Extraction and pre-concentration of uranium using activated carbon impregnated trioctyl phosphine oxide. Elix Appl Chem 100:3462–43469

Ahmad Alyosef H, Schneider D, Wassersleben S, et al (2015) Meso/Macroporous Silica from Miscanthus, Cereal Remnant Pellets, and Wheat Straw. ACS Sustain Chem Eng 3:2012–2021. https://doi.org/10.1021/acssuschemeng.5b00275

Ali SH, Emran MY, Gomaa H (2021) Rice Husk-Derived Nanomaterials for Potential Applications. Waste Recycl Technol Nanomater Manuf 541–588

Atout H, Bouguettoucha A, Chebli D, et al (2017) Integration of Adsorption and Photocatalytic Degradation of Methylene Blue Using TiO 2 Supported on Granular Activated Carbon. Arab J Sci Eng 42:1475–1486. https://doi.org/10.1007/s13369-016-2369-y

Balapure A, Ganesan R (2021) Anatase versus Triphasic TiO2: Near-identical synthesis and comparative structure-sensitive photocatalytic degradation of methylene blue and 4-chlorophenol. J Colloid Interface Sci 581:205–217. https://doi.org/https://doi.org/10.1016/j.jcis.2020.07.096

Bharti V, Vikrant K, Goswami M, et al (2019) Biodegradation of methylene blue dye in a batch and continuous mode using biochar as packing media. Environ Res 171:356–364. https://doi.org/https://doi.org/10.1016/j.envres.2019.01.051

Chougan M, Ghaffar SH, Al-Kheetan MJ, Gecevicius M (2020) Wheat straw pre-treatments using

587 eco-friendly strategies for enhancing the tensile properties of bio-based polylactic acid
588 composites. Ind Crops Prod 155:112836.
589 https://doi.org/https://doi.org/10.1016/j.indcrop.2020.112836

590 Chowdhury A-N, Rahim A, Ferdosi YJ, et al (2010) Cobalt–nickel mixed oxide surface: A promising
591 adsorbent for the removal of PR dye from water. Appl Surf Sci 256:3718–3724.
592 https://doi.org/https://doi.org/10.1016/j.apsusc.2010.01.013

593 Cui J, Cui L, Cheng F, et al (2015) A green route for preparation of low surface area SiO2
594 microspheres from wheat straw ash with activated carbon and NPK compound fertilizer as by-
595 products. RSC Adv 5:80238–80244. https://doi.org/10.1039/C5RA14622D

596 De Gisi S, Lofrano G, Grassi M, Notarnicola M (2016) Characteristics and adsorption capacities of
597 low-cost sorbents for wastewater treatment: A review. Sustain Mater Technol 9:10–40.
598 https://doi.org/https://doi.org/10.1016/j.susmat.2016.06.002

599 Diaz C, Valenzuela ML, Cifuentes-Vaca O, et al (2020) Iridium nanostructured metal oxide, its
600 inclusion in silica matrix and their activity toward photodegradation of methylene blue. Mater
601 Chem Phys 252:123276. https://doi.org/https://doi.org/10.1016/j.matchemphys.2020.123276

602 Emran MY, El-Safty SA, Selim MM, Shenashen MA (2021) Selective monitoring of ultra-trace
603 guanine and adenine from hydrolyzed DNA using boron-doped carbon electrode surfaces.
604 Sensors Actuators B Chem 329:129192.
605 https://doi.org/https://doi.org/10.1016/j.snb.2020.129192

606 Eren MŞA, Arslanoğlu H, Çiftçi H (2020) Production of microporous Cu-doped BTC (Cu-BTC)
607 metal-organic framework composite materials, superior adsorbents for the removal of methylene
608 blue (Basic Blue 9). J Environ Chem Eng 8:104247.
609 https://doi.org/https://doi.org/10.1016/j.jece.2020.104247

610 Gomaa H, El-Safty S, Shenashen MA, et al (2018) Three-Dimensional, Vertical Platelets of ZnO
611 Carriers for Selective Extraction of Cobalt Ions from Waste Printed Circuit Boards. ACS Sustain

612 Chem Eng 6:13813–13825. https://doi.org/10.1021/acssuschemeng.8b01906

613 Gomaa H, Shenashen MA, Elbaz A, et al (2021) Mesoscopic engineering materials for visual
614 detection and selective removal of copper ions from drinking and waste water sources. J Hazard
615 Mater 406:124314. https://doi.org/https://doi.org/10.1016/j.jhazmat.2020.124314

616 Gupta VK, Moradi O, Tyagi I, et al (2016) Study on the removal of heavy metal ions from industry
617 waste by carbon nanotubes: Effect of the surface modification: a review. Crit Rev Environ Sci
618 Technol 46:93–118. https://doi.org/10.1080/10643389.2015.1061874

619 Hassan AA, Sajid M, Tanimu A, et al (2021) Removal of methylene blue and rose bengal dyes from
620 aqueous solutions using 1-naphthylammonium tetrachloroferrate (III). J Mol Liq 322:114966.
621 https://doi.org/https://doi.org/10.1016/j.molliq.2020.114966

622 Ibrahim I, Belessiotis G V., Arfanis MK, et al (2020) Surfactant effects on the synthesis of redox
623 bifunctional v2o5 photocatalysts. Materials (Basel). 13:1–13

624 Islam MT, Dominguez A, Turley RS, et al (2020) Development of photocatalytic paint based on TiO2
625 and photopolymer resin for the degradation of organic pollutants in water. Sci Total Environ
626 704:135406. https://doi.org/https://doi.org/10.1016/j.scitotenv.2019.135406

627 Itteboina R, Sau TK (2019) Sol-gel synthesis and characterizations of morphology-controlled Co3O4
628 particles. Mater Today Proc 9:458–467.
629 https://doi.org/https://doi.org/10.1016/j.matpr.2019.02.176

630 Ji W, Tang Q, Shen Z, et al (2020) The adsorption of phosphate on hydroxylated alpha-SiO2 (0 0 1)
631 surface and influence of typical anions: A theoretical study. Appl Surf Sci 501:144233.
632 https://doi.org/10.1016/j.apsusc.2019.144233

633 Karuppusamy I, Samuel MS, Selvarajan E, et al (2021) Ultrasound-assisted synthesis of mixed
634 calcium magnesium oxide (CaMgO2) nanoflakes for photocatalytic degradation of methylene
635 blue. J Colloid Interface Sci 584:770–778.
636 https://doi.org/https://doi.org/10.1016/j.jcis.2020.09.112

637 Li P, Zhuang Z, Zhang Z, et al (2021) Interfacial heterojunction construction by introducing Pd into
638 W18O49 nanowires to promote the visible light-driven photocatalytic degradation of
639 environmental organic pollutants. J Colloid Interface Sci 590:518–526.
640 https://doi.org/https://doi.org/10.1016/j.jcis.2021.01.067

641 Mezan SO, Absi SM Al, Jabbar AH, et al (2021) Synthesis and characterization of enhanced silica
642 nanoparticle (SiO2) prepared from rice husk ash immobilized of 3-(chloropropyl)
643 triethoxysilanea. Mater Today Proc 42:2464–2468.
644 https://doi.org/https://doi.org/10.1016/j.matpr.2020.12.564

645 Mohamed A, Yousef S, Ali Abdelnaby M, et al (2017) Photocatalytic degradation of organic dyes and
646 enhanced mechanical properties of PAN/CNTs composite nanofibers. Sep Purif Technol
647 182:219–223. https://doi.org/https://doi.org/10.1016/j.seppur.2017.03.051

648 Naing HH, Wang K, Li Y, et al (2020) Sepiolite supported BiVO4 nanocomposites for efficient
649 photocatalytic degradation of organic pollutants: Insight into the interface effect towards
650 separation of photogenerated charges. Sci Total Environ 722:137825.
651 https://doi.org/https://doi.org/10.1016/j.scitotenv.2020.137825

652 Nemiwal M, Zhang TC, Kumar D (2021) Recent progress in g-C3N4, TiO2 and ZnO based
653 photocatalysts for dye degradation: Strategies to improve photocatalytic activity. Sci Total
654 Environ 767:144896. https://doi.org/https://doi.org/10.1016/j.scitotenv.2020.144896

655 Nordin AH, Ahmad K, Kai Xin L, et al (2021) Efficient adsorptive removal of methylene blue from
656 synthetic dye wastewater by green alginate modified with pandan. Mater Today Proc 39:979–
657 982. https://doi.org/https://doi.org/10.1016/j.matpr.2020.04.564

658 Norouzi A, Nezamzadeh-Ejhieh A, Fazaeli R (2021) A Copper(I) oxide-zinc oxide nano-catalyst
659 hybrid: Brief characterization and study of the kinetic of its photodegradation and
660 photomineralization activities toward methylene blue. Mater Sci Semicond Process 122:105495.
661 https://doi.org/https://doi.org/10.1016/j.mssp.2020.105495

662 Phan A, Cole DR, Striolo A (2014) Preferential adsorption from liquid water-ethanol mixtures in
663 alumina pores. Langmuir 30:8066–8077. https://doi.org/10.1021/la501177t

664 Rahman KH, Kar AK (2020) Effect of band gap variation and sensitization process of polyaniline
665 (PANI)-TiO2 p-n heterojunction photocatalysts on the enhancement of photocatalytic
666 degradation of toxic methylene blue with UV irradiation. J Environ Chem Eng 8:104181.
667 https://doi.org/https://doi.org/10.1016/j.jece.2020.104181

668 Ramasamy R, Ramachandran K, Philip GG, et al (2015) Design and development of Co3O4/NiO
669 composite nanofibers for the application of highly sensitive and selective non-enzymatic glucose
670 sensors. RSC Adv 5:76538–76547. https://doi.org/10.1039/C5RA11739A

671 Rani B, Punniyakoti S, Sahu NK (2018) Polyol asserted hydrothermal synthesis of SnO2
672 nanoparticles for the fast adsorption and photocatalytic degradation of methylene blue cationic
673 dye. New J Chem 42:943–954. https://doi.org/10.1039/c7nj03341a

674 Sayed A, Othman IMM, Hamam M, et al (2021) A novel fluorescent sensor for fast and highly
675 selective turn-off detection of Fe3+ in water and pharmaceutical samples using synthesized
676 azopyrazole-benzenesulfonamide derivative. J Mol Struct 1225:129175.
677 https://doi.org/https://doi.org/10.1016/j.molstruc.2020.129175

678 Seaf El-Nasr TA, Gomaa H, Emran MY, et al (2021) Recycling of Nanosilica from Agricultural,
679 Electronic, and Industrial Wastes for Wastewater Treatment. Waste Recycl Technol Nanomater
680 Manuf 325–362

681 Seera SDK, Kundu D, Gami P, et al (2021) Synthesis and characterization of xylan-gelatin cross-
682 linked reusable hydrogel for the adsorption of methylene blue. Carbohydr Polym 256:117520.
683 https://doi.org/https://doi.org/10.1016/j.carbpol.2020.117520

684 Shaban M, Ahmed AM, Shehata N, et al (2019) Ni-doped and Ni/Cr co-doped TiO2 nanotubes for
685 enhancement of photocatalytic degradation of methylene blue. J Colloid Interface Sci 555:31–
686 41. https://doi.org/https://doi.org/10.1016/j.jcis.2019.07.070

687 Sharma PK, Singh MK, Sharma GD, Agrawal A (2021) NiO nanoparticles: Facile route synthesis,
688 characterization and potential towards third generation solar cell. Mater Today Proc 43:3061–
689 3065. https://doi.org/https://doi.org/10.1016/j.matpr.2021.01.400

690 Singh J, Juneja S, Soni RK, Bhattacharya J (2021) Sunlight mediated enhanced photocatalytic activity
691 of TiO2 nanoparticles functionalized CuO-Cu2O nanorods for removal of methylene blue and
692 oxytetracycline hydrochloride. J Colloid Interface Sci 590:60–71.
693 https://doi.org/https://doi.org/10.1016/j.jcis.2021.01.022

694 Soni S, Bajpai PK, Mittal J, Arora C (2020) Utilisation of cobalt doped Iron based MOF for enhanced
695 removal and recovery of methylene blue dye from waste water. J Mol Liq 314:113642.
696 https://doi.org/https://doi.org/10.1016/j.molliq.2020.113642

697 Sun H (1998) Compass: An ab initio force-field optimized for condensed-phase applications -
698 Overview with details on alkane and benzene compounds. J Phys Chem B 102:7338–7364.
699 https://doi.org/10.1021/jp980939v

700 Sun H, Jin Z, Yang C, et al (2016) COMPASS II: extended coverage for polymer and drug-like
701 molecule databases. J Mol Model 22:1–10. https://doi.org/10.1007/s00894-016-2909-0

702 Sun L, Shao Q, Zhang Y, et al (2020) N self-doped ZnO derived from microwave hydrothermal
703 synthesized zeolitic imidazolate framework-8 toward enhanced photocatalytic degradation of
704 methylene blue. J Colloid Interface Sci 565:142–155.
705 https://doi.org/https://doi.org/10.1016/j.jcis.2019.12.107

706 Zhai S, Li M, Wang D, et al (2019) In situ loading metal oxide particles on bio-chars: Reusable
707 materials for efficient removal of methylene blue from wastewater. J Clean Prod 220:460–474.
708 https://doi.org/https://doi.org/10.1016/j.jclepro.2019.02.152

709 Zhang H, Wang C, Zhang W, et al (2021) Nitrogen, phosphorus co-doped eave-like hierarchical
710 porous carbon for efficient capacitive deionization. J Mater Chem A 9:12807–12817.
711 https://doi.org/10.1039/D0TA10797B

712 Zhou L, Yu Q, Cui Y, et al (2017) Adsorption properties of activated carbon from reed with a high
713 adsorption capacity. Ecol Eng 102:443–450.
714 https://doi.org/https://doi.org/10.1016/j.ecoleng.2017.02.036

715